Type: TUTORIAL PAPER
Section: SENSOR AND PHOTONICS DEVICES

Spectral modeling of resonant photonic integrated circuits: tutorial

Modelamiento espectral de circuitos fotónicos integrados resonantes: tutorial

Juan José Arango (1,2,*) and Pedro Torres (1,2)

1. Escuela de Física, Universidad Nacional de Colombia – Sede Medellín.

2. Miembro de la Sociedad Red Colombiana de Óptica.

(*) E-mail: jujarangour@unal.edu.co

Received: 17/01/2022 Accepted: 27/02/2022 DOI: 10.7149/OPA.55.1.51102

ABSTRACT:

Current developments in integrated photonics require the design of new integrated structures and the execution of multiple optimization cycles, for which accessible and flexible modeling techniques represent essential tools. Commonly used in engineering for modeling complex systems, transfer matrices are simple and powerful tools that may be implemented for the simulation of circuit- and system-level photonic elements. In this tutorial, we present a detailed description of a modeling methodology based on signal-flow graphs and transfer matrices that successfully predicts the spectral behavior of resonant photonic circuits. Every stage of the modeling process is comprehensively elaborated in the tutorial, with the aim that it serves as a starting guide for new researchers in the field. Validation results are presented for demonstrating the accuracy of the model in reproducing published benchmarks, and several studies are carried out to illustrate model's scope. In addition to the basic theoretical and practical considerations required for the construction of photonic circuit models, an open-source Python-based software is provided, enabling the immediate implementation of described techniques and their use as baseline for advanced studies and designs.

Key words: Photonic integrated circuit; spectral modeling; signal-flow graph; transfer matrix; open-source software.

RESUMEN:

Los desarrollos actuales en fotónica integrada requieren el diseño de nuevas estructuras integradas y la ejecución de múltiples ciclos de optimización, para lo cual técnicas de modelamiento accesibles y flexibles representan herramientas esenciales. Comúnmente utilizadas en ingeniería para el modelamiento de sistemas complejos, las matrices de transferencia son instrumentos simples y poderosos que pueden implementarse en la simulación de elementos fotónicos a nivel de circuito y sistema. En este tutorial presentamos una descripción detallada de una metodología de modelamiento basada en grafos de flujo de señal y matrices de transferencia que predice exitosamente el comportamiento espectral de circuitos fotónicos resonantes. Cada etapa del proceso de modelamiento se detalla exhaustivamente en el tutorial, con la intención de que este sirva como guía introductoria para nuevos investigadores en el área. Se presentan resultados de validación demostrando la exactitud del modelo para reproducir resultados publicados de referencia, y se realizan varios estudios ilustrando el alcance del modelo. En adición a las consideraciones básicas teóricas y prácticas requeridas para la construcción de modelos de circuitos fotónicos, se provee un software de acceso abierto basado en Python, permitiendo la implementación inmediata de las técnicas descritas y su uso como punto de partida para estudios y diseños avanzados.

Palabras clave: Circuito fotónico integrado; modelamiento espectral; grafo de flujo de señal; matriz de transferencia; software de acceso abierto.



REFERENCES AND LINKS / REFERENCIAS Y ENLACES

- [1] G. Lifante, *Integrated Photonics: Fundamentals*. Chichester, John Wiley & Sons, Ltd. (2003).
- [2] L. Chrostowski, M. Hochberg, *Silicon Photonics Design: From Devices to Systems*. Cambridge, Cambridge University Press (2015).
- [3] A. Rahim, T. Spuesens, R. Baets, W. Bogaerts, "Open-access silicon photonics: current status and emerging initiatives", Proc IEEE **106(12)**, 2313-2330 (2018).
- [4] A. Y. Liu, J. Bowers, "Photonic integration with epitaxial III–V on silicon", IEEE J Sel Top Quantum Electron **24(6)**, 1-12 (2018).
- [5] H. Li, G. Balamurugan, M. Sakib, J. Sun, J. Driscoll, R. Kumar, H. Jayatilleka, H. Rong, J. Jaussi, B. Casper, "A 112 Gb/s PAM4 silicon photonics transmitter with microring modulator and CMOS driver", J Light Technol **38(1)**, 131-138 (2020).
- [6] M. Glick, N. C. Abrams, Q. Cheng, M. Y. Teh, Y. H. Hung, O. Jimenez, S. Liu, Y. Okawachi, X. Meng, L. Johansson, M. Ghobadi, L. Dennison, G. Michelogiannakis, J. Shalf, A. Liu, J. Bowers, A. Gaeta, M. Lipson, K. Bergman, "PINE: photonic integrated networked energy efficient datacenters (ENLITENED Program)", J Opt Commun Netw 12(12), 443-456 (2020).
- [7] M. Dubrovsky, M. Blevins, S. V. Boriskina, D. Vermeulen, "High contrast cleavage detection", Opt Lett **46(11)**, 2593-2596 (2021).
- [8] G. Ruiz-Vega, M. Soler, L. M. Lechuga, "Nanophotonic biosensors for point-of-care COVID-19 diagnostics and coronavirus surveillance", J Phys Photonics **3(1)**, 011002 (2021).
- [9] M. J. Goodwin, G. A. J. Besselink, F. Falke, A. S. Everhardt, J. J. L. M. Cornelissen, J. Huskens, "Highly sensitive protein detection by asymmetric Mach–Zehnder interferometry for biosensing applications", ACS Appl Bio Mater **3(7)**, 4566-4572 (2020).
- [10] J. Notaros, M. Notaros, M. Raval, C. V. Poulton, M. J. Byrd, N. Li, Z. Su, E. S. Magden, E. Timurdogan, T. Dyer, C. Baiocco, T. Kim, P. Bhargava, V. Stojanovic, M. R. Watts, "Integrated optical phased arrays: LiDAR, augmented reality, and beyond", OSA Advanced Photonics Congress 2019, paper IM4A.2 (2019).
- [11] W. Bogaerts, D. Pérez, J. Capmany, D. A. B. Miller, J. Poon, D. Englund, F. Morichetti, A. Melloni, "Programmable photonic circuits", Nature **586**, 207–216 (2020).
- [12] B. J. Shastri, A. N. Tait, T. Ferreira de Lima, W. H. P. Pernice, H. Bhaskaran, C. D. Wright, P. R. Prucnal, "Photonics for artificial intelligence and neuromorphic computing", Nat Photonics 15, 102–114 (2021).
- [13] K. Y. Yang, J. Skarda, M. Cotrufo, A. Dutt, G. H. Ahn, M. Sawaby, D. Vercruysse, A. Arbabian, S. Fan, A. Alù, J. Vučković, "Inverse-designed non-reciprocal pulse router for chip-based LiDAR", Nat Photonics 14, 369–374 (2020).
- [14] X. Qiang, X. Zhou, J. Wang, C. M. Wilkes, T. Loke, S. O'Gara, L. Kling, G. D. Marshall, R. Santagati, T. C. Ralph, J. B. Wang, J. L. O'Brien, M. G. Thompson, J. C. F. Matthews, "Large-scale silicon quantum photonics implementing arbitrary two-qubit processing", Nat Photonics 12, 534–539 (2018).
- [15] W. Bogaerts, L. Chrostowski, "Silicon photonics circuit design: methods, tools and challenges", Laser Photonics Rev **12(4)**, 1700237 (2018).
- [16] L. Vivien, C. Baudot, F. Bœuf, B. Szelag, C. Alonso-Ramos, D. Benedikovic, D. Marris-Morini, E. Cassan, S. Guerber, M. Douix, L. Virot, P. Rodriguez, F. Nemouchi, C. Jany, B. B. Bakir, X. Le Roux, D. Perez-Galacho, M. Berciano, G. Marcaud, I. Charlet, L. Deniel, C. Lafforgue, J. Zhang, S. Serna, P. Damas, P. T. Do, D. Doser, J. Durel, E. Ghegin, V. Vakarin, J. M. Ramirez, S. Monfray, S. Cremer, E. Duran-Valdeiglesias, L. Sanchez, F. Fournel, P. Brianceau, K. Hassan, "Chapter One Building blocks of silicon photonics", Semicond Semimet 101, 1-41 (2019).
- [17] M. Smit, X. Leijtens, H. Ambrosius, E. Bente, J. van der Tol, B. Smalbrugge, T. de Vries, E. J. Geluk, J. Bolk, R. van Veldhoven, L. Augustin, P. Thijs, D. D'Agostino, H. Rabbani, K. Lawniczuk, S. Stopinski, S. Tahvili, A. Corradi, E. Kleijn, D. Dzibrou, M. Felicetti, E. Bitincka, V. Moskalenko, J. Zhao, R. Santos, G. Gilardi, W. Yao, K. Williams, P. Stabile, P. Kuindersma, J. Pello, S. Bhat, Y. Jiao, D. Heiss, G. Roelkens, M. Wale, P. Firth, F. Soares, N. Grote, M. Schell, H. Debregeas, M. Achouche, J. L. Gentner, A. Bakker, T. Korthorst, D. Gallagher, A. Dabbs, A. Melloni, F. Morichetti, D. Melati, A. Wonfor, R. Penty, R. Broeke, B. Musk, D. Robbins, "An introduction to InP-based generic integration technology", Semicond Sci Technol 29, 083001 (2014).



- [18] W. Bogaerts, P. De Heyn, T. Van Vaerenbergh, K. De Vos, S. K. Selvaraja, T. Claes, P. Dumon, P. Bienstman, D. Van Thourhout, R. Baets, "Silicon microring resonators", Laser Photonics Rev **6(1)**, 47-73 (2012).
- [19] Z. Yao, K. Wu, B. X. Tan, J. Wang, Y. Li, Y. Zhang, A. W. Poon, "Integrated silicon photonic microresonators: emerging technologies", IEEE J Sel Top Quantum Electron **24(6)**, 5900324 (2018).
- [20] O. B. Helgason, F. R. Arteaga-Sierra, Z. Ye, K. Twayana, P. A. Andrekson, M. Karlsson, J. Schröder, V. Torres-Company, "Dissipative solitons in photonic molecules", Nat Photonics **15**, 305–310 (2021).
- [21] K. Liao, X. Hu, T. Gan, Q. Liu, Z. Wu, C. Fan, X. Feng, C. Lu, Y. C. Liu, Q. Gong, "Photonic molecule quantum optics", Adv Opt Photonics 12(1), 60-134 (2020).
- [22] G. Cao, S. Dong, L. M. Zhou, Q. Zhang, Y. Deng, C. Wang, H. Zhang, Y. Chen, C. W. Qiu, X. Liu, "Fano resonance in artificial photonic molecules", Adv Optical Mater **8(10)**, 1902153 (2020).
- [23] O. Schwelb, "Generalized analysis for a class of linear interferometric networks—part I: analysis", IEEE Trans Microw Theory Tech **46(10)**, 1409 1418 (1998).
- [24] J. K. S. Poon, J. Scheuer, S. Mookherjea, G. T. Paloczi, Y. Huang, A. Yariv, "Matrix analysis of microring coupled-resonator optical waveguides", Opt Express **12(1)**, 90-103 (2004).
- [25] J. Wu, T. Moein, X. Xu, D. J. Moss, "Advanced photonic filters based on cascaded Sagnac loop reflector resonators in silicon-on-insulator nanowires", APL Photonics 3, 046102 (2018).
- [26] K. Okamoto, Fundamentals of Optical Waveguides. Burlington, Academic Press (2006).
- [27] V. Van, *Optical Microring Resonators : Theory, Techniques, and Applications.* Boca Raton, CRC Press (2017).
- [28] Z. Zheng, M. Iqbal, J. Liu, "Dispersion characteristics of SOI-based slot optical waveguides", Opt Commun **281(20)**, 5151-5155 (2008).
- [29] D. V. Strekalov, C. Marquardt, A. B. Matsko, H. G. L. Schwefel, G. Leuchs, "Nonlinear and quantum optics with whispering gallery resonators", J Opt 18(12), 123002 (2016).
- [30] M. Heiblum, J. Harris, "Analysis of curved optical waveguides by conformal transformation", IEEE J Quantum Electron 11(2), 75 83 (1975).
- [31] D. R. Rowland, J. D. Love, "Evanescent wave coupling of whispering gallery modes of a dielectric cylinder", IEE Proc J **140(3)**, 177 188 (1993).
- [32] S. L. Chuang, "A coupled-mode theory for multiwaveguide systems satisfying the reciprocity theorem and power conservation", J Light Technol **5(1)**, 174 183 (1987).
- [33] J. Willems, J. Haes, R. Baets, "The bidirectional mode expansion method for two-dimensional waveguides: the TM case", Opt Quantum Electron 27, 995–1007 (1995).
- [34] M. A. Tran, T. Komljenovic, J. C. Hulme, M. L. Davenport, J. E. Bowers, "A robust method for characterization of optical waveguides and couplers", IEEE Photonics Technol Lett **28(14)**, 1517–1520 (2016).
- [35] A. Yariv, "Universal relations for coupling of optical power between microresonators and dielectric waveguides", Electron Lett **36(4)**, 321–322 (2000).
- [36] D. G. Rabus, *Integrated Ring Resonators : The Compendium*. Heidelberg, Berlin, Springer (2007).
- [37] M. Bahadori, M. Nikdast, S. Rumley, L. Y. Dai, N. Janosik, T. Van Vaerenbergh, A. Gazman, Q. Cheng, R. Polster, K. Bergman, "Design space exploration of microring resonators in silicon photonic interconnects: impact of the ring curvature", J Light Technol 36(13), 2767 2782 (2018).
- [38] S. Dwivedi, T. Van Vaerenbergh, A. Ruocco, T. Spuesens, P. Bienstman, P. Dumon, W. Bogaerts, "Measurements of effective refractive index of SOI waveguides using interferometers", Integrated Photonics Research, Silicon and Nanophotonics 2015, paper IM2A.6 (2015).
- [39] W. Chen, Z. Wang, W. Chen, Y. J. Chen, "General ring-resonator analysis and characterization by characteristic matrix", J Light Technol **23(2)**, 915–922 (2005).
- [40] P. Saeung, P. P. Yupapin, "Generalized analysis of multiple ring resonator filters: modeling by using graphical approach", Optik **119(10)**, 465–472 (2008).
- [41] IEEE Circuits and Systems Society, IEEE standards on circuits: Definitions of terms for linear signal flow graphs. Standard, IEEE (1960).
- [42] S. J. Mason, H. J. Zimmermann, *Electronic Circuits, Signals, and Systems*. Cambridge, MIT Press (1968).



- [43] X. Zhang, D. Huang, X. Zhang, "Transmission characteristics of dual microring resonators coupled via 3×3 couplers", Opt Express **15(21)**, 13557–13573 (2007).
- [44] P. Sah, *Integrated Photonics Filters with Distributed Bragg Reflector in Silicon-on-Insulator*. PhD thesis, Indian Institute of Technology Madras (2018).
- [45] X. Chen, P. Stroobant, M. Pickavet, W. Bogaerts, "Graph representations for programmable photonic circuits", J Light Technol **38(15)**, 4009–4018 (2020).
- [46] G. F. M. Rezende, *Projeto, caracterização e análise de microrressonadores óticos acoplados em plataforma SOI*. Master thesis, Universidad Estadual de Campinas (2015).
- [47] S. Ploeg, H. Gunther, R. M. Camacho, "Simphony: an open-source photonic integrated circuit simulation framework", Comput Sci Eng 23, 65-74 (2021).
- [48] J. J. Arango, "Molecule Designer software", Zenodo, https://doi.org/10.5281/zenodo.5832007.
- [49] J. J. Arango, "Molecule Designer", GitHub, https://github.com/juanjosearango/Molecule-Designer.
- [50] M. Zhang, C. Wang, Y. Hu, A. Shams-Ansari, T. Ren, S. Fan, M. Lončar, "Electronically programmable photonic molecule", Nat Photonics 13, 36–40 (2019).
- [51] Y. Li, F. Abolmaali, K. W. Allen, N. I. Limberopoulos, A. Urbas, Y. Rakovich, A. V. Maslov, V. N. Astratov, "Whispering gallery mode hybridization in photonic molecules", Laser Photonics Rev **11(2)**, 1600278 (2017).
- [52] Q. Xu, S. Sandhu, M. L. Povinelli, J. Shakya, S. Fan, M. Lipson, "Experimental realization of an on-chip all-optical analogue to electromagnetically induced transparency", Phys Rev Lett **96**, 123901 (2006).
- [53] R. Boeck, N. A. F. Jaeger, N. Rouger, L. Chrostowski, "Series-coupled silicon racetrack resonators and the Vernier effect: theory and measurement", Opt Express 18(24), 25151-25157 (2010).

1. Introduction

Integrated photonics is a flourishing industry and research field that harness modern optoelectronics maturity, forefront techniques in nanotechnology, and installed microelectronics infrastructure, to transfer the extensive available knowledge in photonic science to the development of devices and systems that fully operate on photonic integrated chips [1, 2]. The growing availability of these integrated platforms has enabled the extension of photonic technology capacities and the consequent amplification of their impact, since they provide an ideal setting for the construction of applications with high hardware density demands, strict control of external conditions and strong reliance on light-matter interaction; also streamlining the conversion of prototypes into commercial products, by scaling up the fabrication reproducibility and reducing the costs per device [3, 4]. Many integrated photonic technologies are already serving society, in different areas, such as data communication [5, 6], medical monitoring and diagnosis [7-9], or augmented reality [10], and new promising application fields are under active development [11-14].

However, in order to meet the expectations posed on next generations of integrated devices, overcoming several technical barriers is essential. For instance, constraints derived from the strong reliance of circuit performance on small fabrication errors need to be relaxed, the compatibility of different material platforms and the possibility of transitioning towards different frequency bands need to be enabled, and novel devices meeting the exigent demands of the ongoing quantum revolution need to be developed. These open challenges raise interests on the generation of integrated solutions in both the device and circuit levels, and require the conception, design and optimization of new structures and architectures. For contributing to this process, simulation and modeling tools are required for the assessment and tuning of proposed solutions performance [15], which motivates the presentation of this tutorial that aims to provide technical orientation and an open-source design tool that could facilitate further studies on these systems. The model employed in this tutorial is derived from a semi-analytical approach and takes advantage of a signal-flow graph-assisted technique, which simplifies the systematic integration of independent transfer matrix-based descriptions of multiple individual components. The tutorial is intended to serve as baseline for researchers starting projects in the field, as it details the theoretical framework and practical strategies upon which the proposed design workflow is supported, provides access to the photonic design software used for the generation of presented results, and suggests an extensive set of literature resources for further reference.



Among the wide set of components used in the composition of photonic integrated circuits (PIC) [16, 17], photonic resonators are traditional devices, pervasively used in the design of conventional and new solutions due to their high sensitivity and capacities for power concentration, spectral filtering and signal processing [18, 19]. Their versatility and areas of application have been broadened by means of the composition of resonant structures comprising multiple coupled resonators (i.e., photonic molecules) [20-22]. Current interest in the study and exploitation of this kind of circuits has been taken into consideration, hence the focus on resonant structures of this work.

Recent progress in nanophotonics has extended the variety of integrated resonators that may serve as specialized cavities, intended for specific advanced tasks. The consideration of these sophisticated structures is possible under the scope of this work if their optical behavior is accurately described by transfer matrices [23]. Nevertheless, our approach is primarily dedicated to complex resonant systems made up of conventional integrated structures, supplied by most of PIC foundries and whose fabrication is already refined. Three of these systems are shown in Figure 1 and will be presented as study cases throughout the tutorial. Figure 1(a) illustrates a coupled-resonator optical waveguide (CROW), which consists of a set of serially coupled microring resonators, that is waveguide-coupled at both ends. This system has several output ports. In this work we will analyze the signal obtained at the end of the power supply waveguide, commonly known as through port, and the one obtained at the opposite-side waveguide's facet that receives most of the decoupled power, known as drop port. Figure 1(b) presents a cascaded Sagnac loop reflectors (CSLR) resonator. It is made up of a series of reflectors like the one presented in Figure 2(a), whose mirror character is provided by the evanescent coupler at the bottom of the loop. Figure 1(c) illustrates an array of coupled microring resonators in a flower-like configuration in which there is effective coupling between all adjacent resonators. This flower-like system is laterally waveguide-coupled for power supply and signal probing. CROW and CSLR study cases take the studies conducted by Poon et. al. [24] and Wu et. al. [25] as benchmarks for model validation purposes. Thereby, circuits parameters have been set accordingly.

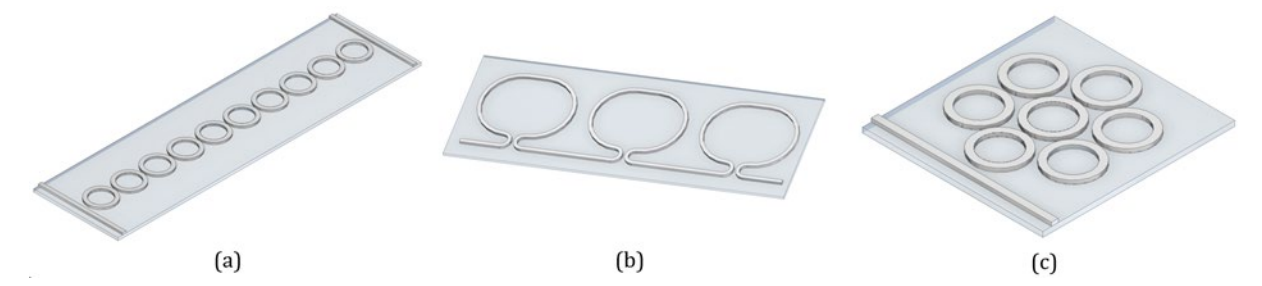


Fig. 1. Examples of photonic integrated circuits, used as study cases throughout this tutorial. (a) Coupled-resonator optical waveguide. (b) Cascaded Sagnac loop reflectors resonator. (c) Flower-like photonic molecule.

These study cases are taken as common thread for presenting a complete modeling workflow, going from the basic theoretical considerations to the use of an in-house software for the realization of different spectral analyses. In this way, Section 2 presents the analytical descriptions of basic photonic components that are used later to build more complex systems; Section 3 describes a numerical methodology for obtaining the parameters that characterize each basic component; Section 4 introduces the concept of signal-flow graph as an ancillary structure to systematize the analysis of arbitrary designs and its use for computing photonic circuit's stationary state; Section 5 provides the instructions for getting access to the open software published along with this work; and Section 6 discusses the obtained results on the spectral behavior of studied systems, providing a general outlook of the scope of the model. Conclusions are included at the end, summarizing the highlights of the tutorial.

2. Building blocks models

This tutorial concentrates on resonant circuits comprising rectangular waveguides and evanescent couplers; thereby, their operation can be easily decomposed in the contributions of these basic components, as suggested by the diagram presented in Figure 2. Theoretical models are presented below for these components, which are used in section 4 as building blocks for the construction of entire circuits descriptions.





Fig. 2. (a) Integrated Sagnac loop reflector. (b) Integrated Sagnac loop reflector schematically broken down into its basic components: waveguides and couplers.

For the sake of clarity and general practicality, several assumptions are made to simplify the presentation of the main concepts, while focusing on the operation conditions more commonly preferred. In this way, linear, passive, single-mode and stationary operation is assumed for all the waveguides. In addition, materials are considered to have low dispersion and frequency-independent losses, which may be directly assumed in narrowband studies. These conditions may appear to be very restrictive, but the operating regimes of many integrated photonic technologies comply with them. In any case, the model can be upgraded while preserving the same approach for taking into account the coupling of the fundamental mode with high-order modes, or by introducing the information of frequency-dependent material properties. Thus, this tutorial may serve as basis for the further development of more sophisticated models, tailored according to research or technology needs.

2.a. Waveguides.

Integrated waveguides are planar photonic structures, whose dielectric profile allows the confinement of light via total internal reflection, and rectangular waveguides are the most common choice for photonic integrated circuits (Figure 3). To have an accurate description of their contribution to the integrated circuit behavior it is relevant to study the phase-shift and power attenuation rates that guided light experiences.

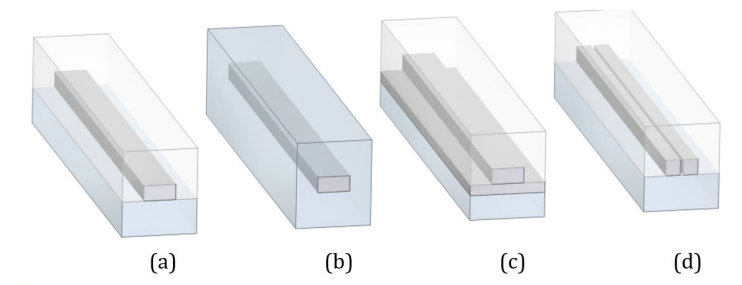


Fig. 3. Planar waveguides examples. (a) Strip waveguide. (b) Buried strip waveguide. (c) Rib waveguide. (d) Slot waveguide.

According to their properties, waveguides only provide effective guiding to a specific set of supported modes, associated with geometric configurations of the electromagnetic field that ensure the replication of the wave as it propagates (i.e., self-consistency condition), imposing fixed relations between spatial and temporal periodicity of the radiation (i.e., dispersion relations). Waveguide propagation modes thus appear as eigenvectors of the eigenvalue problem that arises from the establishment of the continuity relations and the dielectric profile of the guiding structure in the application of Maxwell's equations for solutions that preserve their transversal configuration [26]. For lossless straight waveguides, these solutions have the following form for the transversal field:

$$\vec{\mathcal{E}}_T(x, y, z, t) = \vec{E}_T(x, y)e^{-i\beta z}e^{i\omega t} = A(z)\vec{e}_T(x, y)e^{i\omega t},\tag{1}$$

where A(z), β and ω are the complex amplitude of the propagating mode, its propagation constant, and light signal frequency, respectively. $\vec{\mathbf{e}}_T(x,y)$ is the normalized vector function that stores the information about mode's characteristic polarization distribution.

With $\vec{E}_{\mathrm{T}}(x,y) = E_x \hat{x} + E_y \hat{y}$, the quasi-TE and quasi-TM modes of the eigenvalue problem can be formulated as follows [27]:



$$\frac{\partial}{\partial x} \left(\frac{1}{n^2(x, y)} \frac{\partial}{\partial x} (n^2(x, y) E_x) \right) + \frac{\partial^2 E_x}{\partial y^2} + n^2(x, y) k_0^2 E_x = \beta_{TE}^2 E_x, \tag{2}$$

$$\frac{\partial}{\partial y} \left(\frac{1}{n^2(x,y)} \frac{\partial}{\partial y} \left(n^2(x,y) E_y \right) \right) + \frac{\partial^2 E_y}{\partial x^2} + n^2(x,y) k_0^2 E_y = \beta_{TM}^2 E_y; \tag{3}$$

where $k_0=2\pi/\lambda_0$ represents the wavenumber, λ_0 is the vacuum wavelength, and n(x,y) corresponds to the refractive index profile. It is clear that ω and β are characteristic quantities that inform about the temporal and spatial phase-shift rate of the mode. Therefore, their ratio stores the information about the effective phase velocity at which modal wavefronts propagate. Then, it is natural that the effective index of the mode is defined as

$$n_{\text{eff}} \coloneqq \frac{c}{(\omega/\beta)} = \frac{\beta}{k_0},\tag{4}$$

being $v_p = \omega/\beta$ the modal phase velocity. For certain propagation length L, the evolution of the phase of the guided mode can be calculated as

$$\Delta \varphi = \beta L = n_{\text{eff}} k_0 L. \tag{5}$$

Both β and n_{eff} can be used to unambiguously identify certain mode, and their relationship with frequency (i.e., dispersion) may be engineered by adjusting waveguide materials properties or geometry [28].

In relation to power attenuation, modes may lose their carried energy via different mechanisms. Thus, losses can have absorptive, scattering, and radiative nature. Linear absorption is associated with the ordinary interaction of light with the material and will be as low as material transparency allows within the operation frequency band. Scattering losses are provoked by fabrication defects, namely, impurities or surface roughness; thereby, their intervention in device operation is modelled stochastically. Radiative losses are associated with light decoupling from the guiding structure as a consequence of disturbances in the confining dielectric profile, such as bends or the presence of new structures near to the waveguide core. The contributions of these loss mechanisms to power decay can be included into a single attenuation coefficient α as [29]

$$\alpha = \alpha_{abs} + \alpha_{scat} + \alpha_{rad} \,. \tag{6}$$

As a result, the evolution of the complex amplitude associated to an attenuated single-mode propagation in a waveguide is described by

$$A(L) = A_0 e^{i\Delta\phi} e^{-\alpha L} = A_0 e^{i(\beta + i\alpha)L} = A_0 e^{i\tilde{\beta}L}, \tag{7}$$

which entails a Beer-Lambert power decay and a harmonic phase progression. To obtain a more condensed formulation of the modal propagation description, a generalized complex propagation constant is commonly defined as $\tilde{\beta} = \beta + i\alpha$, whose real and imaginary parts account for the mode phase evolution and amplitude attenuation rates, respectively.

If waveguides are bent, they keep the capacity of guiding their eigenmodes, whose wavefronts rotate as they propagate so that the traveling direction remains parallel to the walls of the waveguide. It is worth to remark that the perturbation introduced by the bend alters the effective index and confinement capacity of the structure, implying that the modes of bent waveguides have an intrinsic lossy character [27, 30]. In consequence, radii of curvature should be designed large enough to avoid significant deviations of the effective index and loss rate of the straight counterpart. Considering that this condition needs to be fulfilled in the design processes covered by this tutorial, the mismatch between straight and bent waveguides effective indices will be disregarded, and if the radiative losses associated to the bends are significant, they may be included into the waveguide attenuation coefficient (equation 6).



2.b. Couplers.

Integrated couplers are used for transferring power from one waveguide to another. This is usually performed by approaching a waveguide to the vicinity to the other, so that the evanescent fields of the propagation mode supported by the waveguide can reach the core of the neighbor waveguide and serve as a channel that supplies optical power [31], in analogy with tunnelling effects between quantum wells. The electromagnetic details of the interplay between coupled waveguide modes can be described from several approaches, such as Coupled Mode Theory [32] and Eigenmode Expansion Methods [33]. However, even if the coupler was analytically, numerically or experimentally characterized, the information of its operation can be encoded in transfer matrices [34]. In this approach, incoming and outgoing waveguides are treated as input and output ports of a linear system and get related by scalar values stored in the transfer matrix (T-matrix) associated to the coupler. Complex amplitudes of signals at each port of a coupler, as the one shown in Figure 4, are thus related by the T-matrix presented in equation (8).

$$\begin{bmatrix} a_{1_{out}} \\ a_{2_{out}} \end{bmatrix} = \mathbf{T} \begin{bmatrix} a_{1_{in}} \\ a_{2_{in}} \end{bmatrix} = \begin{bmatrix} T_{11} & T_{12} \\ T_{21} & T_{22} \end{bmatrix} \begin{bmatrix} a_{1_{in}} \\ a_{2_{in}} \end{bmatrix}. \tag{8}$$

T-matrix elements are not independent, but the relationships they hold are determined by the requirements of energy conservation and reciprocity, whose implications are briefly elaborated below.

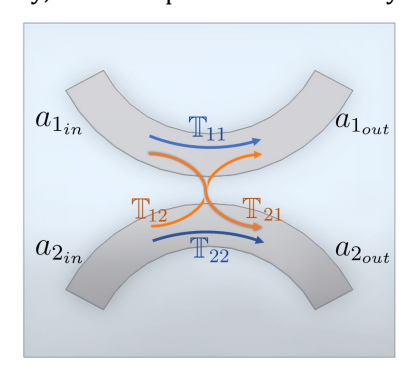


Fig. 4. 2×2 evanescent coupler. Depicted arrows and transfer factors indicate the relations between the complex amplitudes of output and input signals.

If the coupler is assumed to be lossless, power balance provides the first relation between coupled modes amplitudes:

$$\sum_{j=1,2} P_{j_{in}} = \sum_{j=1,2} P_{j_{out}}, \qquad (9)$$

$$\left|a_{1_{in}}\right|^{2} + \left|a_{2_{in}}\right|^{2} = \left|a_{1_{out}}\right|^{2} + \left|a_{2_{out}}\right|^{2}.$$
 (10)

Reciprocity implies that if output fields were time-reversed, light would be assembled back into original (reversed) input fields. This is possible if \mathbf{T} is invertible, so that

$$\begin{bmatrix} a_{1_{in}} \\ a_{2_{in}} \end{bmatrix} = \mathbf{T}^{-1} \begin{bmatrix} a_{1_{out}} \\ a_{2_{out}} \end{bmatrix} = \frac{1}{\det(\mathbf{T})} \begin{bmatrix} T_{22} & -T_{12} \\ -T_{21} & T_{11} \end{bmatrix} \begin{bmatrix} a_{1_{out}} \\ a_{2_{out}} \end{bmatrix}, \quad (T_{11}T_{22} - T_{12}T_{21}) \neq 0.$$
 (11)

If $a_{1_{out}}$ and $a_{2_{out}}$ are replaced in (10) by using the relation with $a_{1_{in}}$ and $a_{2_{in}}$ given by (8), and $a_{1_{in}}$ and $a_{2_{in}}$ are replaced in (10) by using the relation with $a_{1_{out}}$ and $a_{2_{out}}$ given by (11), the following constraints are found

$$|T_{11}|^2 = |T_{22}|^2; |T_{12}|^2 = |T_{21}|^2;$$
 (12)

$$\phi_{11} + \phi_{22} = 2p\pi; \quad \phi_{12} + \phi_{21} + \pi = 2q\pi;$$
 (13)

$$T_{11}T_{22} - T_{12}T_{21} = 1; (14)$$



where p and q are integers, and $\phi_{jk} = Arg\{T_{jk}\}$. A similar derivation is presented in the appendix of reference [31].

These conditions that T-matrix entries have to fulfill are summarized in the T-matrix formulation [35]

$$\mathbf{T} = \begin{bmatrix} t & \kappa \\ -\kappa^* & t^* \end{bmatrix}, |t|^2 + |\kappa|^2 = 1, (t, \kappa \in \mathcal{C}).$$
 (15)

As explained in [36], a simplified form of equation (15) can be obtained from the assumption that the phase induced by the coupling is symmetrical between waveguides, so that T-matrix can be presented as

$$\mathbf{T} = \begin{bmatrix} t & i\kappa \\ i\kappa & t \end{bmatrix}, \ t^2 + \kappa^2 = 1, \ (t, \kappa \in \Re e).$$
 (16)

Since coupler transmission and coupling coefficients, t and κ , are bound, determining one of these will provide enough information for characterizing the lossless coupling between identical waveguides. This is the type of coupler that will be assumed in next studies, and a recurrent approximation in integrated circuits modeling.

3. Determination of parameters

The models presented in section 2 establish how the design parameters of modelled devices (i.e., α , β and κ) affect their optical behaviour. However, to fabricate a device according to certain design, or to predict the response of an already fabricated device, it is important to connect design parameters with fabrication specifications. To obtain this connection, several strategies can be employed, whose validity depends on the applicability of their assumptions in the context of the studied system.

Multiple analytical approaches have been devised for estimating the dispersion relations of waveguides [26], curvature-induced radiative losses in bends [30], and the coupling coefficients in directional or adiabatic couplers [37]. These approaches make it possible to have a fully analytical solution of the global system, with which the influence of every fabrication parameter can be clearly traced back. However, they usually imply approximations that are held for quite specific configurations, so it is unpractical to rely on these models only.

Other possibility for characterizing the devices is to perform direct experimental measurements that may allow for the parameter extraction [34, 38], certainly the most adequate option for modeling reproducible devices, such as those fabricated in production lines with standardized manufacturing processes. Nevertheless, the execution of these experiments for research purposes entails high costs, is time-consuming and depends on the technological availability of the structures being modelled.

Another alternative for characterizing the building blocks for the circuit design process is to calculate the parameters by running electromagnetic simulations for the devices under consideration. As example of the information that may be obtained following this strategy, the results of several Finite Element Method (FEM) simulations in the frequency domain are presented below.

Figure 5 shows the results of computing the fundamental quasi-TE mode of a rectangular $450 \text{ nm} \times 220 \text{ nm}$ waveguide, with material properties set for silicon-on-insulator (SOI) platform. Figure 5(a) plots the mode effective index against wavelength, and Figure 5(b) illustrates the distribution of the electric field norm of the fundamental mode. A unitary vector field has been superimposed, with the aim of indicating the transverse polarization distribution as well.

Figure 6 presents another numerical study that was performed for obtaining the order of magnitude of the losses introduced by circular bends of different radii. Several bends were arranged serially, and the power output was calculated after stationary propagation throughout 20 bends of 90 degrees, keeping a fixed wavelength value of λ_0 =1.55 µm. This allowed to estimate the loss associated to every 90°-turn. From Figure 6(a) it is possible to infer that the losses increase exponentially as the radius of curvature is reduced. Figure 6(b) shows the electric field norm distribution, and it is evident that for the smaller radius case the losses are more notorious (the same color scale was used for both visualizations).



For coupling coefficient estimation, a pair of circularly bent waveguides were simulated as they were located at different relative distances. As expected, as the gap increases the coupling ratio attained decays exponentially. Another relevant variable to take into consideration is the radius of coupled bends, since larger radii allow the interaction of the two modes to be effective along longer distances. Figure 7(a) presents the results of power transmission obtained at the output port, indicating the amount of power that was decoupled from the supply waveguide. The relationships of coupling efficiency with gap and curvature radius are evident. Figure 7(b) shows the electric field norm distribution for couplers with different gaps, preserving a radius of 10 μ m.

Electric field norm distributions (Fig. 5-7) remain valid for any input power. Thus, color scales are arbitrary.

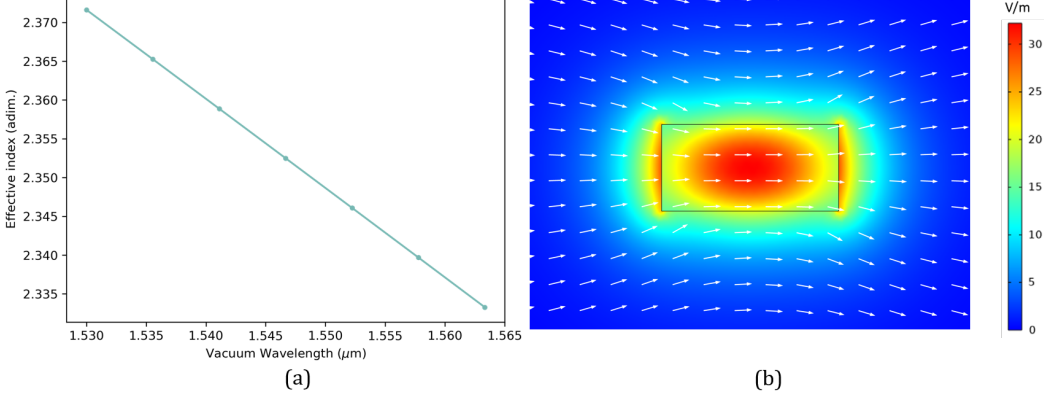


Fig. 5. FEM simulation results for the transverse field of the quasi-TE mode of a rectangular SOI strip buried waveguide. (a) Effective index dependence on mode's frequency (vacuum wavelength). (b) Electric field norm and transverse polarization distributions.

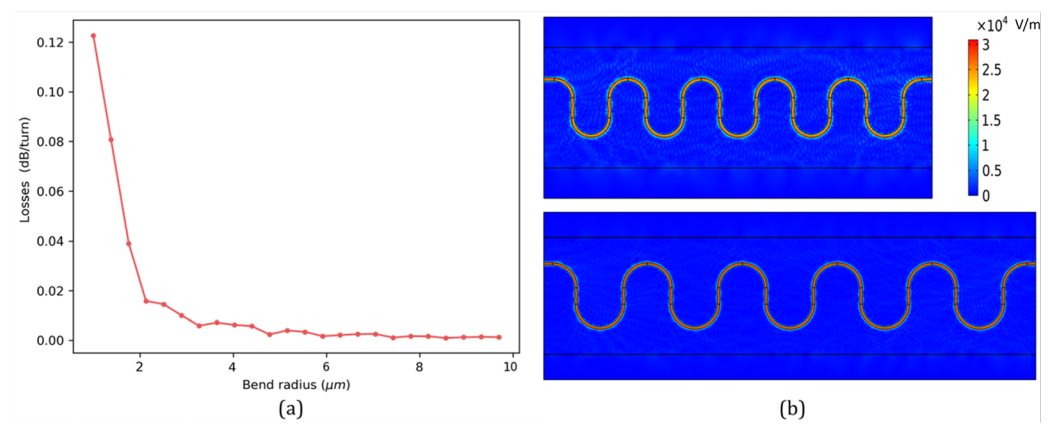


Fig. 6. FEM simulation results for losses in SOI meandering waveguides (λ_0 =1.55 µm). (a) Bend losses (dB/turn) dependence on bend curvature. (b) Electric field norm distribution of light propagating throughout meandering waveguides with 2.51 µm radius of curvature (upper) and 4.02 µm radius of curvature (lower).

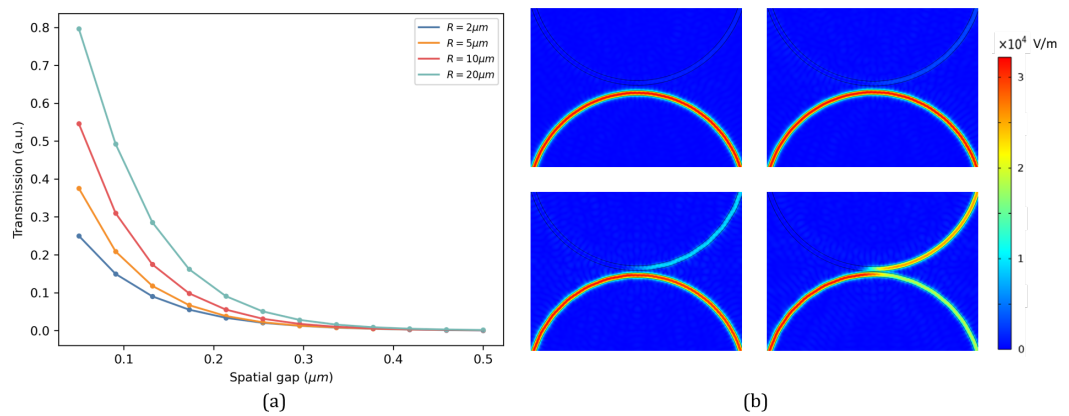


Fig. 7. FEM simulation results for coupling efficiency of a coupler comprising two coupled waveguide bends with identical radius of curvature (λ_0 =1.55 µm). (a) Dependence of the decoupled power on separation gap and radius of curvature. Power transmission is normalized with respect to the input signal, hence the use of arbitrary units (a.u.). (b) Electric field norm distribution of light at coupler with 10 µm radius of curvature and separation gap of 459 nm, 377 nm, 173 nm and 50 nm (from upper left to lower right).



4. Signal-flow graphs and adjacency matrices

Having established the models accounting for individual components, the global operation of the circuit (i.e., the global transfer function) can be obtained by linking all the local transfer conditions, which are provided by the transfer equations of all the building blocks that the circuit comprises. If all conditions are simultaneously imposed in an extended equation system, its solution would represent the complex amplitudes of the signal flowing within the photonic circuit at stationary regime. Instead of proceeding with a direct algebraic procedure, it is convenient to define a graph-based general workflow, aiming at developing a systematic protocol for the analysis of circuits with arbitrary design, suited for developing a software design tool. Besides, the use of graph structures for encoding photonic circuit properties paves the way for further model upgrades that may exploit graph theory concepts and algorithms.

Signal-flow graphs are graphical representations of systems, especially suitable for signal evolution studies. Commonly used for solving electrical, control and automation engineering problems, they have also been applied in the modeling of photonic circuits and systems [39, 40], as they offer a useful scalar way of tracking optical signal amplitude and phase. Signal-flow graphs represent modelled devices by decomposing them into discrete evaluation points, represented as graph vertices, or nodes, at which the signal is locally evaluated. The nodes are chosen in a way such that the signal transfer relations between nodes are independent, so that the transferred signal from a node to another relies only on signal's evaluation at the starting node. All nodes sharing an allowed signal-flow path, are connected by directed edges, or branches, whose associated complex-valued weight and orientation determine the signal transfer relation and flow direction respectively [41, 42]. Transfer relations are in general complex-valued functions and may be parametrized by device design specifications. Transfer functions between two nodes, referred below as local transfer functions, are defined as the quotient of the complex amplitudes of the optical signal evaluated in such nodes. For our purposes, waveguides and couplers ports will be used as evaluation nodes.

The *translation* of the photonic basic elements within the graph-based framework is illustrated in Figure 8. Single-mode waveguides may be represented by single directed edges, as shown in Figure 8(a), having associated a weight accounting for the corresponding phase and amplitude evolution coefficients, given by (5), (6) and (7). Figure 8(b) shows the graph representation for couplers, similar to the one presented in section 2.b (see Figure 4). Additional structures are displayed in Figure 8(c), namely, a three-waveguide coupler and an integrated distributed Bragg reflector (DBR). These are common components in integrated photonic circuits, and they may be characterized with a T-matrix, as demonstrated in [43] and [44]. Thus, they may be incorporated in signal-flow graph models as well, but their study is out of the scope of this work.

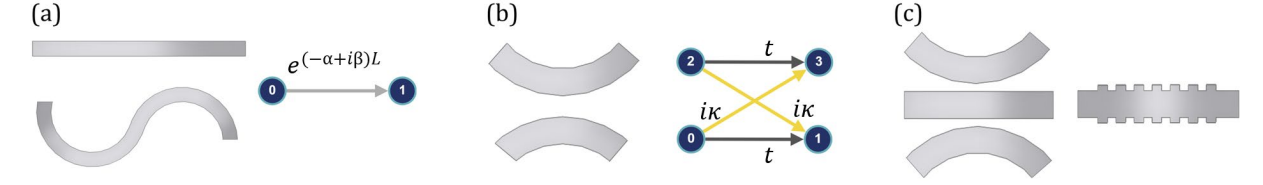


Fig. 8. Basic photonic components and equivalent graph elements. (a) Single-mode waveguides are modelled by single directed edges. (b) Unidirectional couplers are modelled as symmetric crossbar-like arrangement of directed edges. (c) Examples of other signal-flow graph-compatible photonic components, not included in the analysis carried out in this tutorial.

The integration of previous basic graph elements allows the composition of much more complex structures, such as the resonators under analysis. In this way, the signal-flow graph for the Sagnac reflector, presented and conceptually fragmented in Figure 2, is obtained by representing its basic photonic components with their corresponding graph-equivalent elements, as shown in Figure 9. This chart shows that when counterpropagating modes are allowed by the system, the ports of the basic photonic components have associated a duplicate number of nodes, so that counterpropagating signal-flows get represented by different branches, connecting different nodes.



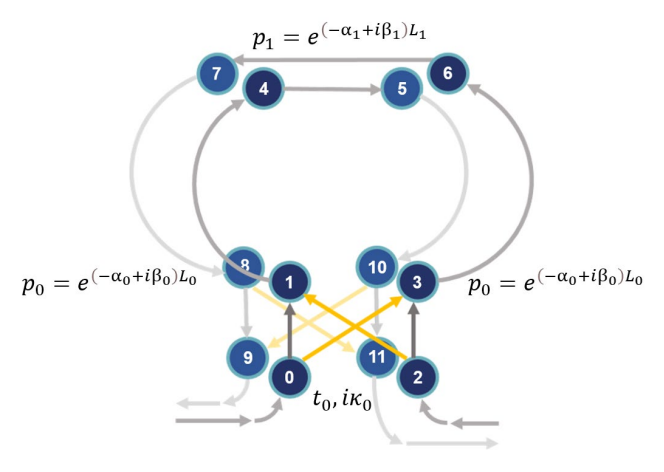


Fig. 9. Signal-flow graph representation of a Sagnac loop reflector. It is necessary to duplicate vertices for ports allowing counterpropagating signals, so that their information gets stored in independent graph branches.

Following this procedure, the signal-flow graphs for the photonic circuits under consideration (Figure 1) are illustrated in Figure 10. Every edge of these graphs has an associated weight determined by the design parameters of the circuit, which are in principle independent. With the purpose of alleviating the visualization, bidirectional edges are used to denote counterpropagation segments (Figures 10(b) and 10(c)), keeping in mind that formal calculations require the unfolded format already described (Figure 9), and node numbering has been omitted. It is worth to remark that the use of graphs with antiparallel directed edges connecting the same pair of nodes is not a suitable modeling alternative for counterpropagating flows, since doing so leads to unphysical light reversal events [45].

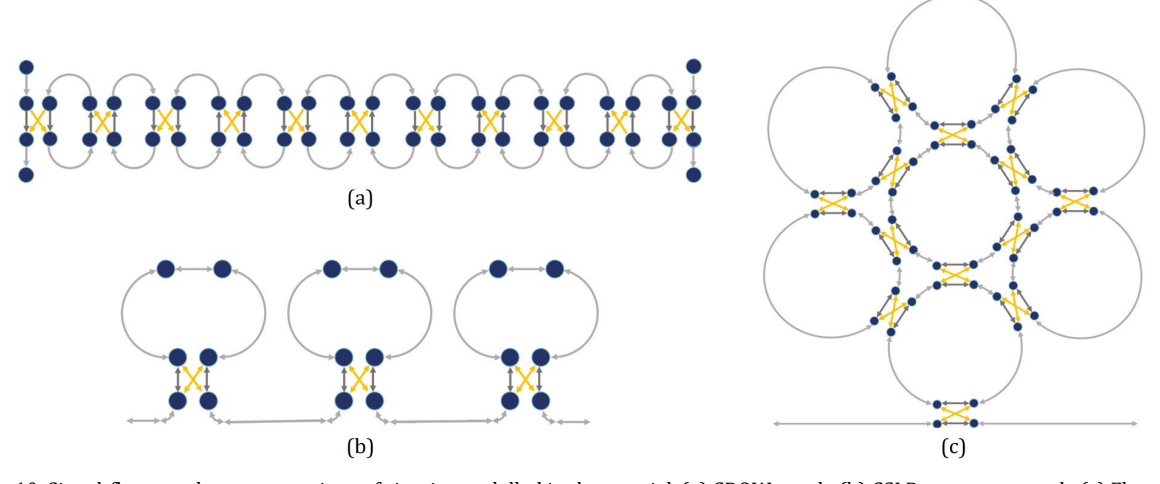


Fig. 10. Signal-flow graph representations of circuits modelled in the tutorial. (a) CROW graph. (b) CSLR resonator graph. (c) Flower-like photonic molecule graph. Bidirectional edges imply a duplicate number of nodes and edges.

Having defined the graph representing the circuit under study, and the design parameters that characterize the operation of its constitutive components, its global spectral behavior can be obtained by solving the stationary condition for the system, using the adjacency matrix $\bf A$ associated with the graph [46]. This is a mathematical resource used to encode connectivity information of a graph in a square matrix format. It has as many rows and columns as nodes appearing in the graph. According to the numbering convention of the nodes, the n^{th} row and column of the matrix are associated with the n^{th} node of the graph, and its (j,k)-entry $\bf A_{jk}$ corresponds to the complex-valued local transfer function associated with the directed edge starting at the jth node and ending at the kth node. If there is no edge connecting a pair of nodes, the corresponding entry takes a null value. As illustration, the adjacency matrix associated to the graph shown in Figure 9 is presented in Figure 11.



	From / To	0	1	2	3	4	5	6	7	8	9	10	11
	0	ΓO	t_0	0	$i\kappa_0$	0	0	0	0	0	0	0	0 ј
	1	0	0	0	0	p_0	0	0	0	0	0	0	0
	2	0	$i\kappa_0$	0	t_0	0	0	0	0	0	0	0	0
	3	0	0	0	0	0	0	p_0	0	0	0	0	0
	4	0	0	0	0	0	p_1	0	0	0	0	0	0
$\mathbf{A} =$	5	0	0	0	0	0	0	0	0	0	0	p_0	0
	6	0	0	0	0	0	0	0	p_1	0	0	0	0
	7	0	0	0	0	0	0	0	0	p_0	0	0	0
	8	0	0	0	0	0	0	0	0	0	t_0	0	iκ ₀
	9	0	0	0	0	0	0	0	0	0	0	0	0
	10	0	0	0	0	0	0	0	0	0	$i\kappa_0$	0	t_0
	11	Γ0	0	0	0	0	0	0	0	0	0	0	0]

Fig. 11. Adjacency matrix associated to Sagnac loop reflector graph presented in Figure 9.

Thus, the stationary condition fulfilled by the system, after reaching the steady state, can be formulated as

$$\vec{a} = \vec{a}_0 + \mathbf{A}^{\mathrm{T}} \, \vec{a} \,, \tag{17}$$

where \vec{a} and \vec{a}_0 are column vectors, such that the a_j component is the stationary signal amplitude evaluated at the jth node, and the a_{0j} component is the amplitude associated with constant external excitation at the jth node. Equation (17) implies that the superposition of external constant excitation and the image of the state vector under the \mathbf{A}^T transformation (transfer relations) yields the same state vector, hence the stationarity. Taking the transpose of the adjacency matrix is necessary for preserving the conventional notations for adjacency matrices and vector equations.

Solving for the stationary signal amplitude vector \vec{a} , one obtains

$$(\mathbf{I} - \mathbf{A}^{\mathrm{T}}) \, \vec{a} = \vec{a}_{0}; \tag{18}$$

$$\vec{a} = (\mathbf{I} - \mathbf{A}^{\mathrm{T}})^{-1} \, \vec{a}_0; \tag{19}$$

$$\vec{a} = ((\mathbf{I} - \mathbf{A})^{-1})^{\mathrm{T}} \vec{a}_0. \tag{20}$$

In this way, the (j,k)-entry of $\mathbf{T}_c = ((\mathbf{I} - \mathbf{A})^{-1})^{\mathrm{T}}$ stores the global transfer relation from the kth node to the jth node. So, \mathbf{T}_c can be considered a global transfer matrix for the entire circuit.

If a frequency (wavelength) sweep is performed by updating the entries of **A**, computing \vec{a} as ω (λ_0) is varied, the spectral behavior of the system is obtained. Since \vec{a} not only contains information about the output node, but about every node in the defined graph, it is possible to generate the energetic and phase distributions of the signal within the entire circuit for every computed ω (λ_0).

5. Open software

The models detailed in sections 2-4 were employed for developing **Molecule Designer**: A Python-based software that allows to directly calculate the transmittance spectrum and frequency-dependent phase-shift of a photonic circuit. It also allows to generate visualizations of the energetic and phase distributions of light circulating at stationary state within the circuit for any required frequency or wavelength.

Users provide the design specifications of the circuit under study by entering the associated adjacency matrix in a symbolic format (i.e., with every parameter symbolized by a label), so that sweeps can be easily performed in the design space. For the generation of distribution graphics, it is necessary to provide information on the relative positions of graph nodes. It can be made just by providing an image of the graph, and the software will present it in a graphic interface on which users can directly click on the image locations that will be saved as nodes coordinates. Plots generated by Molecule Designer can be interactively displayed or stored in text and image formats. Graphics of distributions can be temporally displayed or stored in PDF files.



The software allows to specify the spectral band for the study and tune the sampling. It allows to select between frequency or wavelength formats for results generation as well. In addition, it is possible to adjust several settings regarding plots and graphics presentation and styles. The general appearance of Molecule Designer, being executed in Spyder (Scientific Python Development Environment), is illustrated in Figure 12.

Molecule Designer was built to be compatible with drag-and-drop circuit design environments. A similar open-source design tool that allows to programmatically generate circuits designs has been developed by Ploeg *et. al.* [47].

Molecule Designer is an open-source code, that may be accessed in Zenodo and GitHub repositories [48, 49]. Moreover, GitHub repository includes basic instructions for the execution and use of the program.

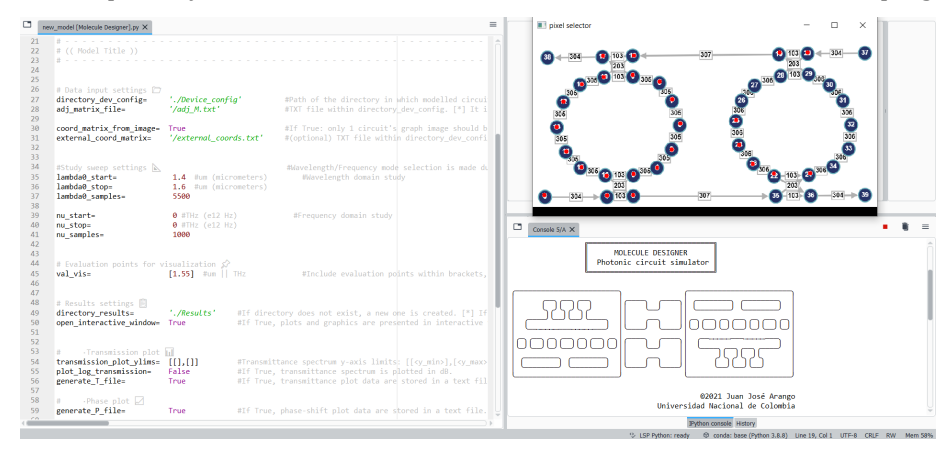


Fig. 12. General outlook of Molecule Designer running on Spyder. Settings panel, graphical coordinate selection window and command line interface are displayed.

6. Results

The application of the described semi-analytical modeling approach enables the execution of multiple studies. Some of them were performed to analyze the spectral response of the photonic devices used as study cases, and the obtained results are discussed below as illustration of the scope of this model. All analyses were obtained with the assistance of the developed software Molecule Designer.

Transfer matrix-based models are well suited for efficiently predicting the effect that variations of some design parameters would have on the performance of the device. This is demonstrated by calculating the spectral transmission and reflection of the cascaded Sagnac loop reflectors resonator and carrying out several parameters sweeps, hence, checking its reliance on coupling coefficients, loss rate, and effective index. It was modelled with fixed geometric parameters and constant coupling coefficient for the central coupler. In this way, the separation between loops and loops' lengths were $d=100~\mu m$ and $l=129.66~\mu m$, respectively (Figure 13(e)). The central coupler transmission coefficient was maintained as t_2 =0.97 for all the sweeps. As expected, the spectra in Figure 13 share the characteristic functional form that results from the mode splitting (i.e., modal hybridization) that occurs for pairs of coupled cavities (dimers) [50]. Figure 13(a) presents the transmission curves predicted for different waveguide effective indices, while keeping losses and coupling ratios constant, with $\alpha = 55 \text{ m}^{-1}$ (0.239 dB/mm) and $t_1 = t_2 = t_3$ =0.97. It is observed that the variation of the effective optical path length of the cavity produced by the effective index sweep shifts the wavelengths at which the resonance condition is fulfilled. In Figure 13(b), the result of varying the attenuation is shown, as α was swept from 500 m⁻¹ to 1300 m⁻¹ (2.171 dB/mm 5.646 dB/mm). In this case, a constant value for the effective index of $n_{\rm eff}=2.5802$ was held, and couplers configuration was $t_1=t_2=$ t_3 =0.97. It is clear from the curves set that both the transmission and peak-valley contrast increase as lower losses are considered. Figures 13(c-d) present the transmission and reflection of the system for different couplers configurations, as the equated transmission coefficients of the outermost reflectors t_1 and t_3 are swept from 0.75 to 0.99, while keeping t_2 =0.97. It is noticeable that by changing the coupling strength, the magnitude of the mode splitting (separation of the peaks) is affected, which is a typical feature of circuits with coupled cavities. Results presented in Figure 13(c) match with those reported by Wu et. al. in [25], in which a cascaded Sagnac loop reflectors resonator with the same characteristics is studied, thus serving as validation of the method described in this tutorial.



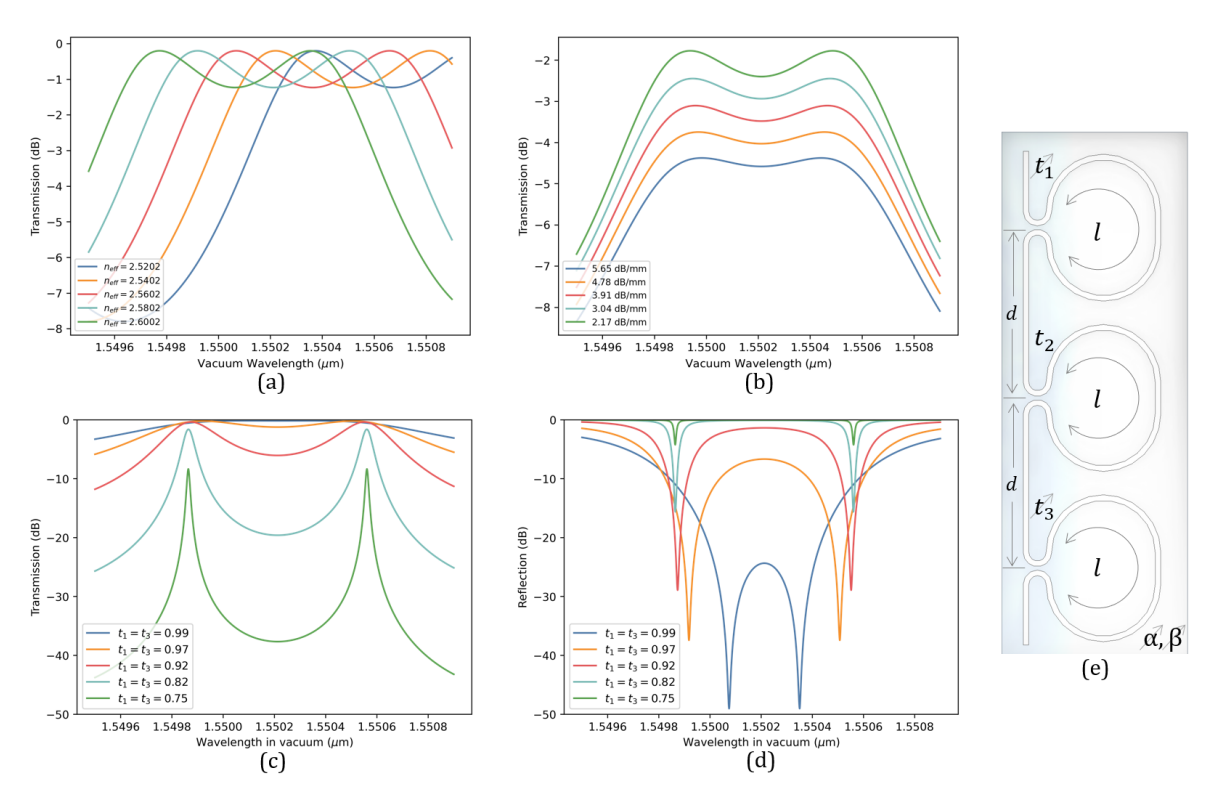


Fig. 13. Transmission and reflection spectra computed for the CSLR resonator for different parameter sweeps. (a) Effective index sweep, keeping $\alpha=55~\mathrm{m}^{-1}$ and $t_1=t_2=t_3$ =0.97 fixed. (b) Attenuation coefficient sweep, keeping $n_{\mathrm{eff}}=2.5802$ and $t_1=t_2=t_3$ =0.97 fixed. (c) Outermost couplers efficiency sweep (transmission), keeping $\alpha=55~\mathrm{m}^{-1}$, $n_{\mathrm{eff}}=2.5802$ and $t_2=0.97$ fixed. (d) Outermost couplers efficiency sweep (reflection), keeping $\alpha=55~\mathrm{m}^{-1}$, $n_{\mathrm{eff}}=2.5802$ and $t_2=0.97$ fixed. (e) Schematic representation of modelled circuit with parameters labels indicated. Separation length between reflectors and their circulation lengths are $d=100~\mathrm{\mu m}$ and $l=129.66~\mathrm{\mu m}$, respectively.

For computing the spectra of the signal at different ports, as made for the reflection calculation in Figure 13(d), it is necessary to consider different nodes of the corresponding graph. Under the followed modeling approach, this just implies an alternation of the considered entry from the computed matrix. This property of the models based on signal-flow graphs can be exploited for evaluating field's power build-up factors in internal sectors of the circuit, for which the optical signal amplitude and phase can be calculated as functions of wavelength. This study was made for the 7-ring flower-like photonic molecule (Figure 1(c)), obtaining the results presented in Figure 14. By selecting different nodes of the graph, through-port transmission, and power build-up factors for clockwise and counter-clockwise propagations in the central microring were calculated. In addition, the phase state of the mode at each evaluation node was also obtained, using as reference the phase state at the entry of the circuit. All resonators were assumed to be identical, with roundtrip length $l=2\pi\cdot(15~\mu\text{m})$, effective index $n_{\text{eff}}=2.8$ and loss rate given by $\alpha=500~\text{m}^{-1}$ (2.171 dB/mm). The flower-like photonic molecule is waveguide-coupled, with a coupling ratio given by $\kappa_0=0.5$, and all the couplers between microrings are designed to have equal ratio, with $\kappa_1 = 0.45$. Figure 14(d) details the location at which the field is analyzed. The spectra in Figure 14 span over a wavelength range that corresponds to one period of the flower-like circuit spectrum, and three periods of the spectra associated to the individual microrings. It is interesting to notice that in contrast with the spectra associated with the topologies of other systems of identical coupled resonators [51], instead of appearing always the same set of supermodes in the vicinity of each individual resonator eigenwavelength, the mode can split in different sets of supermodes, which implies that by coupling microrings in this configuration, the spectrum changes its period. This suggests that this specific topology enables certain types of propagation loops or virtual cavities, with effective round-trip lengths that are not multiples of the individual microring round-trip length. Thus, these circuits would have associated resonance modes with out-of-the-grid periodicities participating in the modal hybridization that produces these spectra. In addition, it is observed from Figure 14(b-c) that the excited supermodes have different power build-up factors for clockwise (CW) and counterclockwise (CCW) propagation for the same location in the circuit. CW signal builds up more power than the CCW one in most of the cases, but certain supermodes circulate throughout the central microring with most of their power going in the CCW direction. For those supermodes with comparable contribution of both CW and CCW propagation, standing waves are expected to appear in the analyzed microring.



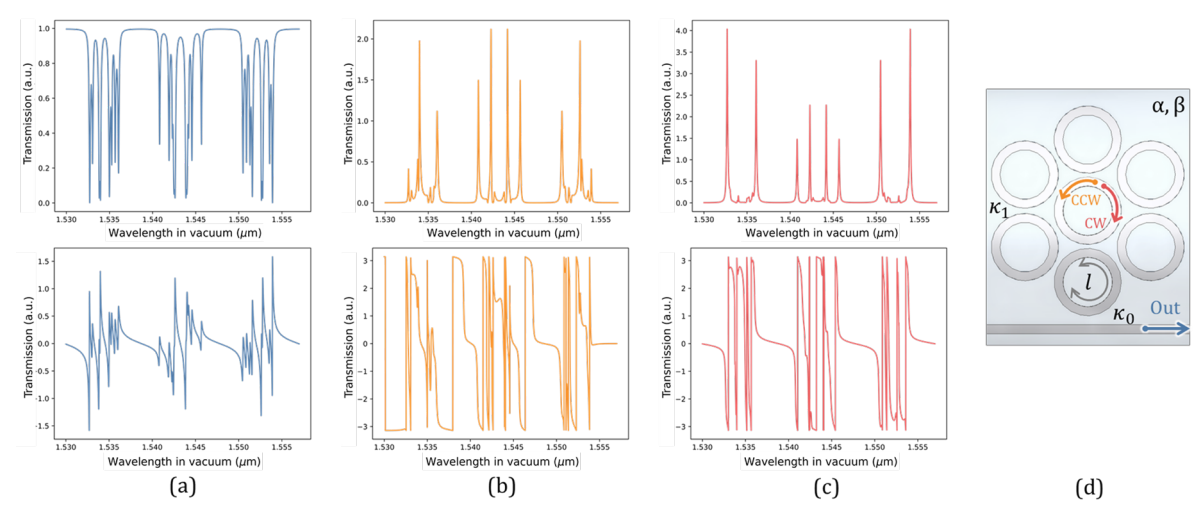


Fig. 14. Stationary light signal spectrally probed at different locations of the flower-like photonic molecule comprising seven identical microrings with round-trip length $l=2\pi\cdot(15~\mu\text{m})$, effective index $n_{\text{eff}}=2.8$ and loss rate given by $\alpha=500~\text{m}^{-1}$. Waveguide-ring and ring-ring coupling efficiency is given by $\kappa_0=0.50$ and $\kappa_1=0.45$, respectively. (a) Transmittance and phase-shift of the signal at output port, normalized with respect to the input signal. (b) Buildup factor and phase-shift attained by counter-clockwise propagation in the central microring, normalized with respect to the input signal. (c) Buildup factor and phase-shift attained by clockwise propagation in the central microring, normalized with respect to the input signal. (d) Schematic representation of modelled circuit with parameters labels and signal probe locations indicated.

It has been demonstrated that the methods described can provide information not just about the outgoing signals, but also about the inner details of the device operation. If the build-up factor is calculated for every node of the graph, it is even possible to generate a map of the irradiance of the light flowing throughout the entire circuit. This was made for the 10-ring CROW, with the aim of displaying the spatial power distribution of each of its resonances. A CROW with similar specifications to the one studied by Poon et. al. in [24] was considered (Figure 15(c)), with identical microrings of effective round-trip length of $l = 2\pi \cdot (164.5 \,\mu\text{m})$, effective index $n_{\rm eff} = 1.4982$, and very low losses given by $\alpha = 1 \times 10^{-9} \, \rm m^{-1}$. The coupling coefficients considered were $\kappa_0=0.5$ and $\kappa_1=0.3$, for the coupling with the waveguides and between rings, respectively. Typical transmission spectra were obtained for through and drop ports. They are presented in Figure 15(a) and Figure 15(b), and clearly show the band-pass filtering nature of the CROW and the appearance of ten supermodes associated to the spectrum local minima (or maxima). By comparing the two spectra, it is possible to identify their complementarity relation, derived from the interferometric origin of CROW's frequency selectivity. The results for spatial power distribution study are presented in Figure 16: the aforementioned irradiance map was generated for each resonance wavelength (Figure 16(b-k)), and an arbitrary out-of-resonance wavelength (Figure 16(a)). The graphical representation of the device exhibits sharp points, as consequence of the discrete character of the graph used to support the model, but it clearly presents the information about the concentration or absence of optical power in every location of the circuit, as it is excited with radiation of different wavelengths. It is evident from Figure 16(a) that when the resonance condition is not fulfilled, light does not get confined in the system, and most of the power is preserved within the supply waveguide. In contrast, when a resonance is reached, the transmission through the supply waveguide is strongly attenuated, by means of the out-of-phase waves that return from the circuit, and the constructive interference that occurs inside of the CROW allows for the confinement of the light within the coupled cavities. Light can resonate forming different spatial configurations that characterize the resonant supermode. Figures 16(b-k) show that these distributions can be symmetrical or anti-symmetrical with respect to the central coupler of the CROW. It is also noticed that every CROW supermode shares the same spatial power distribution with the supermode that is equally shifted with respect to the original eigenwavelength of the individual microrings (i.e., midpoint of the spectral pattern). Color scales for all the irradiance maps have been normalized, so the maximum irradiance in each map gets assigned the maximum color level. Nevertheless, it is possible to verify that supermodes have a different power confinement performance by checking the numeric range indicated on the color scale. It appears that outermost (most red- and blue-shifted) supermodes have the greatest power confinement capacity, as they reach internal irradiance values almost seven times higher than those at the entry port. Besides, supermodes with the same spatial power distribution attain the same irradiance maxima.

Additionally, it is worth to remark that the configurations of spatial power distributions follow a clear complexity pattern: simpler distributions correspond the outermost resonances, and the most complex



correspond to the inner ones. Here complexity is associated with the amount of independent local power maxima. Figure 17 makes this interesting feature more evident by presenting a saturated grayscale version of Figure 16.

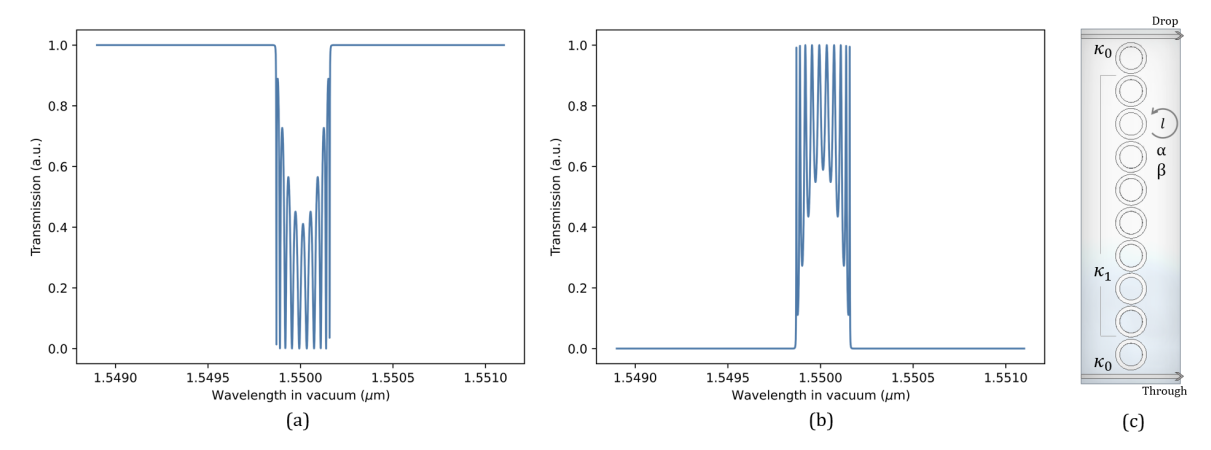


Fig. 15. CROW spectral study results. (a) Transmittance spectrum at through port. (b) Transmittance spectrum at drop port. Power transmission is normalized with respect to the input signal, arbitrary units (a.u.) used. (c) Schematic of modelled circuit with parameters and ports labels indicated. Parameters values: $l=2\pi\cdot 164.5~\mu m$, $n_{\rm eff}=1.4982$, $\alpha=1\times 10^{-9}~m^{-1}$, $\kappa_0=0.5$ and $\kappa_1=0.3$.

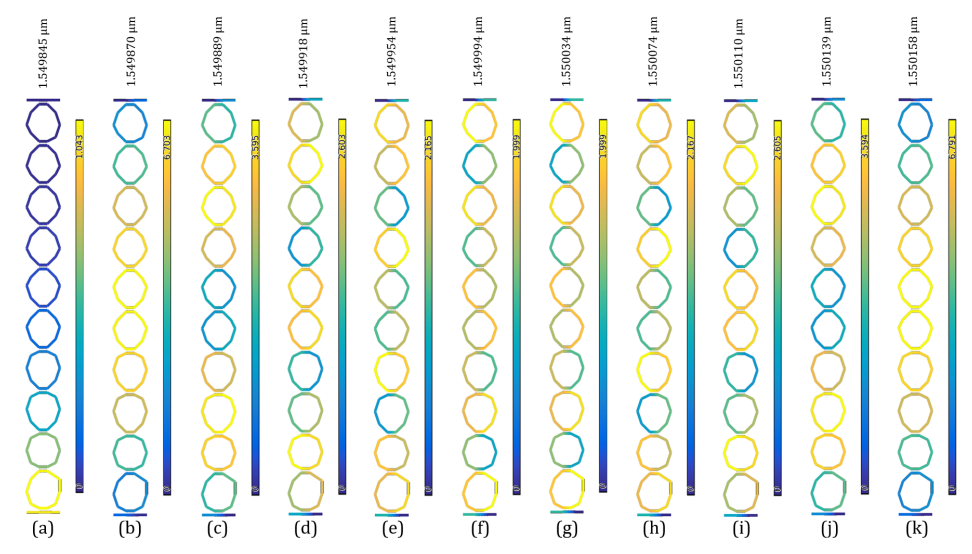


Fig. 16. Electric field norm distribution (in V/m) for CROW operating at (a) out-of-resonance and (b-k) resonance wavelengths. Each resonance wavelength corresponds to a local minimum in through port transmission spectrum (Figure 15(a)).

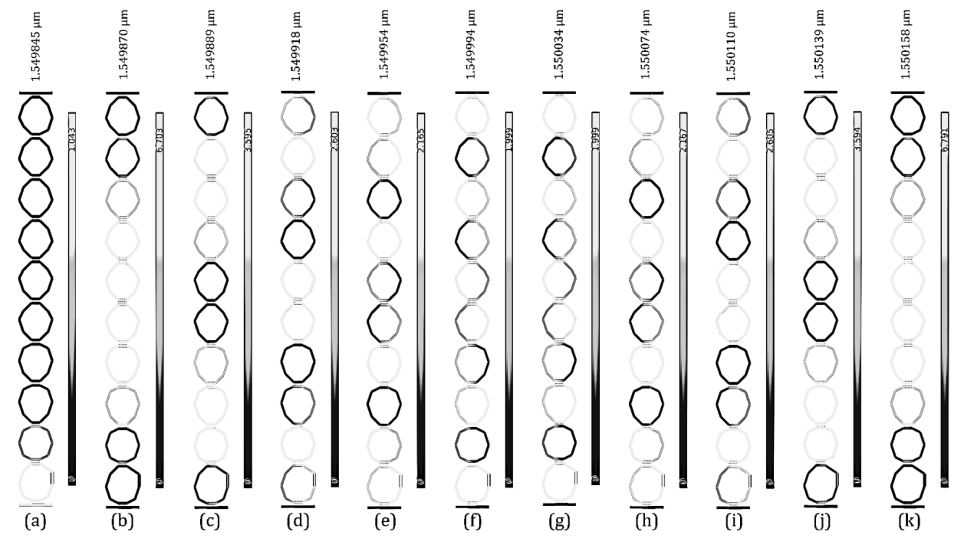


Fig. 17. Grayscale saturated version of Figure 16. Energetic maxima complexity distributions can be observed more clearly. Central supermodes have associated more complex energetic distributions than outermost supermodes.



Previous results have shown some of the different types of studies that the described model allows. These may serve as tools for conducting analyses of new integrated architectures, characterizing device proposals, or finding the parameters for optimal performance of certain structures. As evidence of the capacities of this modeling technique, two additional circuits with interesting phenomena were modelled, accurately reproducing the reported experimental results provided by Xu *et. al.* in [52] and Boeck *et. al.* in [53]. Figure 18(a) shows the spectral transmission of a pair of parallel coupled microrings, whose parameters were adjusted, as indicated in [52] for exhibiting Coupled Resonators Induced Transparency (CRIT) effect. Figure 18(b) presents the drop port transmission of a pair of asymmetrical serially coupled resonators, with effective round-trip lengths adjusted to enable the observation of Vernier effect [53]. These briefly discussed examples illustrate the design possibilities that the modeling methodology can allow. Their corresponding design parameters are summarized in Table 1.

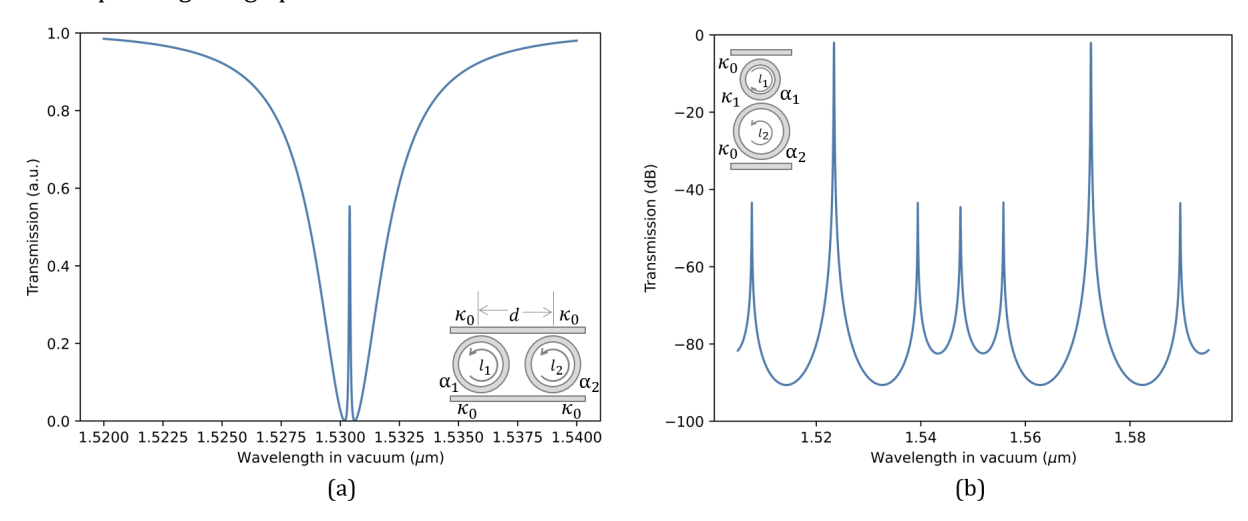


Fig. 18.(a) CRIT effect modeling. Transmittance spectrum at through port of an array of two parallel coupled microrings. Circuit schematic description and parameters labels displayed at inset. Power transmission is normalized with respect to the input signal, hence the use of arbitrary units (a.u.). (b) Vernier effect modeling. Transmittance spectrum at drop port of an array of two serially coupled microrings. Circuit schematic description and parameters labels displayed at inset.

CRIT circuit Vernier circuit Parameter Value Parameter Value $15.71 \, \mu m$ $28.425 \mu m$ d l_1 l_1 $2\pi \cdot 5 \mu m$ $42.637 \mu m$ l_2 $2\pi \cdot 5.0014 \, \mu \text{m}$ l_2 3.4 $n_{
m eff}$ 1.997 69.08 m^{-1} $n_{
m eff}$ α_1 100 m^{-1} 69.08 m^{-1} α_1 α_2 100 m^{-1} 0.122 α_2 κ_0 0.35 0.007 κ_0 κ_1

TABLE 1. Design parameters for CRIT and Vernier circuits.

7. Conclusions

A workflow for modeling resonant integrated photonic circuits comprising planar waveguides and evanescent couplers was presented, describing a semi-analytical approach for developing studies that integrate analytical models of numerically characterized building blocks, by leveraging circuits graph representations. Main theoretical details of basic photonic components descriptions were explained, and the matrix formulation for calculating circuit's stationary behavior was derived. Resonant circuits examples were used as study cases throughout the tutorial for illustrating the realization of every modelling workflow step.



Results for several modeling studies were presented, highlighting different circuits properties that may be analyzed with the described modeling workflow. Most of presented results were validated with previously published results in academic literature.

This tutorial is published along with the in-house python-based software developed for implementing the models. It can be obtained online as an open-access resource for the realization further studies.

Acknowledgments

The authors are grateful to Prof. Samuel Serna, Bridgewater State University, USA, for fruitful discussions and technical advice provided for the preparation of this tutorial.

